

Molecular Dynamics Simulations of Carbon Dioxide Intercalation in Hydrated Na-Montmorillonite

Evgeniy M. Myshakin,^{*,†,‡} Wissam A. Saidi,[§] Vyacheslav N. Romanov,[†] Randall T. Cygan,^{||} and Kenneth D. Jordan^{†,⊥}

[†]National Energy Technology Laboratory, 626 Cochrans Mill Road, Pittsburgh, Pennsylvania 15236, United States

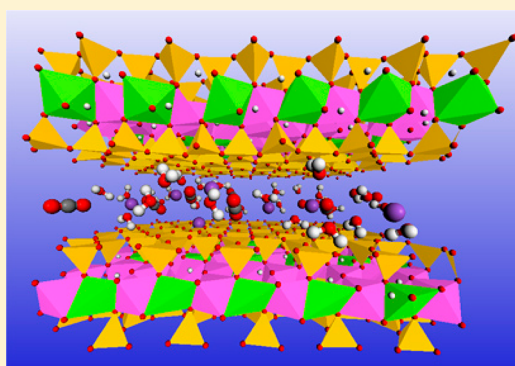
[‡]URS Corporation, P.O. Box 618, South Park, Pennsylvania 15129, United States

[§]Department of Chemical and Petroleum Engineering, University of Pittsburgh, Pittsburgh, Pennsylvania 15261, United States

^{||}Sandia National Laboratories, P.O. Box 5800, Albuquerque, New Mexico 87185, United States

[⊥]Department of Chemistry, University of Pittsburgh, Pittsburgh, Pennsylvania 15260, United States

ABSTRACT: Molecular dynamics simulations using classical force fields were carried out to study the structural and transport properties of clay mineral–water–CO₂ systems at pressure and temperature relevant to geological carbon storage. The simulations show that the degree of swelling caused by intercalation of CO₂ strongly depends on the initial water content in the interlayer space and that CO₂ intercalation stimulates inner-sphere adsorption of the positively charged interlayer ions on the internal clay surfaces, which modifies the wetting properties of the surfaces. DFT-based molecular dynamics simulations were used to interpret the origin of the observed shift in the asymmetric stretch vibration of CO₂ trapped in montmorillonite. The origin of the shift is attributed to the electric field effects on the CO₂ molecules induced by the water molecules.



1. INTRODUCTION

Long-term storage of industrial carbon dioxide in subsurface geological strata is considered a viable option for mitigating greenhouse gas emissions.¹ The technology of geologic carbon dioxide storage involves the injection of supercritical CO₂ (scCO₂) into deep geologic formations such as saline aquifers overlain by sealing cap rocks and geologic traps that would prevent the CO₂ from escaping. The ability of seals to retain injected CO₂ depends on their permeability and geomechanical property evolution.² Cap rocks are often comprised of shale or mudstone enriched with clay minerals, including swelling clays like montmorillonite (MMT).³ MMT is a layered aluminosilicate where the central sheet is composed of octahedrally coordinated Al atoms, and the adjacent sheets contain tetrahedrally coordinated Si atoms. These sheets comprise a 2:1 or tetrahedral–octahedral–tetrahedral (TOT) layer. In MMT, the TOT layers are negatively charged due to substitution of divalent metals (e.g., Mg²⁺ or Fe²⁺) for the octahedrally coordinated Al or by less common substitution of Al for Si at tetrahedral sites. Hydroxyl groups complete the coordination of each octahedra. The negative charge of the TOT layers is counterbalanced by interlayer cations (e.g., Na⁺, Li⁺, Ca²⁺) that are usually hydrated allowing for expansion or contraction of the interlayer distance of the clay depending on the relative humidity.⁴ Swelling clay particles interacting with scCO₂ can also undergo changes in interlayer content and in the basal spacing.^{5,6} This can lead to changes in porosity, permeability, and formation of micro fractures in cap rocks. As

a result, studies of the interactions between scCO₂ and the minerals of cap rocks are necessary for assessing impacts from the long-term exposure of injected CO₂ to geological seals.⁷

Dry scCO₂ injected into a geological aquifer will become hydrated as a result of contact with brine retained at mineral surfaces and nanopores.⁸ The resulting hydrated CO₂ interacts with the cap rocks predominantly through diffusion unless pre-existing or evolved fractures provide pathways for CO₂ migration.⁹ Recently, Giesting et al.⁵ reported *in situ* X-ray diffraction (XRD) characterization of gaseous CO₂ and scCO₂ interacting with Na-rich-MMT at $T = 45\text{ }^{\circ}\text{C}$ and $P = 50\text{--}650$ bar (In experiments, Na-rich-MMT is typically represented by natural or Na-exchanged SWy montmorillonite samples from Wyoming, and Ca-rich-MMT by natural or Ca-exchanged STx montmorillonite samples from Texas; in addition to the prevailing interlayer cations there are differences in the distributions of Mg, Al, and Si within the silicate layers of SWy and STx clay samples, which may complicate interpretation of the results).^{10,11} The study by Giesting et al.⁵ showed that for partially hydrated samples the spacing between the mineral layers (basal d -spacing) expands upon CO₂ adsorption and that the degree of expansion depends on the initial water content in the interlayers. In the absence of CO₂, the basal d -spacing is around 10 Å for nearly dry clay and

Received: December 20, 2012

Revised: April 4, 2013

Published: May 1, 2013

increases to 12.5 Å for a fully saturated monolayer water arrangement (the so-called 1W hydration state characterized with basal d -spacings in the range of 11.5–12.5 Å).^{4,12,13} Upon incorporation of more water, the d -spacing can increase to 14.5–15.5 Å to the next stable state where water forms a bilayer (2W) structure.^{4,12,13} The XRD measurements showed that nearly dry clay displays no significant response upon exposure to dry scCO₂ and that residual water is required to intercalate CO₂.

Maximum expansion upon CO₂ intercalation was found at initial $d = 11.3$ Å resulting in swelling to $d = 12.5$ Å, the value that corresponds to the 1W state. The *in situ* XRD study by Schaefer et al.⁶ on scCO₂ interacting with Ca-MMT at submonolayer water content confirms the expansion of the clay phase to d values corresponding to the 1W state after exposure to dry scCO₂ over a range of temperatures (50–100 °C) and pressures (90, 125, and 180 bar). Interaction of dry scCO₂ with smectite clay in the 2W state results in a collapse of the d -spacing to that of the 1W state.⁶ However, interaction of Na-exchanged SWy and Ca-exchanged STx samples with variably wet scCO₂ (2%–100% saturation of H₂O) at $T = 50$ °C and $P = 90$ bar can lead to swelling to a d -spacing of 18.8 Å values equal to that of the 3W state.^{8,14} Thus, dry scCO₂ has the capacity to dehydrate clay and to promote increase of seal permeability due to clay collapse. On the other hand, the presence of water in scCO₂ can facilitate further swelling of clay.

Loring et al.¹⁵ further confirmed intercalation of CO₂ by means of NMR spectroscopy and attenuated total reflection infrared spectroscopy. They found that intercalated CO₂ molecules are rotationally constrained and do not appear to react with waters to form bicarbonate or carbonic acid.¹⁵ Using diffuse-reflectance infrared spectroscopy, Romanov et al.^{16–19} have analyzed the vibrational fingerprint of CO₂ trapped in SWy and STx samples and also concluded that CO₂ can be intercalated in the interlayers of smectite minerals. These experiments revealed 5–10 cm⁻¹ red shifts of the asymmetric stretch fundamental frequency for the trapped CO₂ relative to that of the gas-phase molecule.¹⁹ CO₂ trapped in clay interlayers is in an intricate environment involving interactions with interlayer ions, water, and clay surfaces. As was shown by Duncan and co-workers^{20–22} the asymmetric stretch fundamental of CO₂ is shifted 10–80 cm⁻¹ to the blue when the molecule forms a complex with metal ions. This observation suggests that it is the interaction with water and/or internal clay surfaces that is responsible for the observed red shift of the asymmetric stretch of CO₂ in interlayers of MMT.

Recently, Botan et al.²³ performed Monte Carlo (MC) and molecular dynamics (MD) simulations of CO₂ intercalation into Na-MMT using a force field for clay from Smith²⁴ and the SPC²⁵ and EMP2²⁶ models for water and carbon dioxide, respectively. Specifically, they considered Na-MMT in equilibrium with H₂O–CO₂ mixtures at $T = 75$ °C and $P = 25$ and 125 bar. Their simulations indicated that hydrated clay can intercalate CO₂ and that the thermodynamically stable structures are characterized with basal d -spacings corresponding to the 1W and 2W hydration states. That is consistent with experiment which shows that exposure of montmorillonite to CO₂ resulted in expansion of clay particles giving the basal d -spacings equal to those values at 1W or 2W.^{5,6} Monte Carlo simulations of nonhydrated Na-MMT clay in equilibrium with dry scCO₂ have shown that CO₂ intercalation is unfavorable until large d -spacing distances (>2W).²⁷ For d -spacings >15.5

Å, the Helmholtz free energy displays a set of closely spaced local minima separated by small barriers.²⁷ Other modeling studies^{28–30} using different force fields also indicate that CO₂ molecules can exist in the interlayers of clay minerals. At the same time, little is known about the molecular details of CO₂ intercalation in the interlayer of smectite clays.

In the present study, classical molecular dynamics simulations are used to elucidate the process of CO₂ intercalation into hydrated Na-MMT at initial water content and P - T conditions relevant to geological formations suitable for CO₂ storage. Of particular interest are the structural and transport properties of interlayer species after carbon dioxide intercalation. In addition, density functional theory (DFT)-based molecular dynamics is engaged to compute vibrational power spectra for comparison with the experimental IR spectra and the power spectra from force field simulations.

2. COMPUTATIONAL DETAILS

2.1. MD Simulations Using Density Functional Theory.

In recent years, computational resources have improved making it possible to tackle complex clay mineral systems by using electronic structure methods. Density functional theory, in particular, provides reliable estimates of electrostatic potentials, thermodynamics, spectroscopic data, reaction mechanisms, and other properties.^{31,32} DFT-based Born–Oppenheimer molecular dynamics (BOMD) simulations were carried out using the CP2K software package.³³ The evolution of a system using BOMD methods is governed by Newtonian dynamics with energies and forces at each time step being estimated from DFT calculations.³⁴ Goedecker–Teter–Hutter pseudopotentials^{35,36} were used together with a hybrid Gaussian-plane wave scheme (GPW) with a DZVP quality Gaussian basis set³⁷ for the Kohn–Sham orbitals and an energy cutoff of 350 Ry for the plane-wave expansion of the electron density. The gradient-corrected correlation functional of Perdew, Burke, and Ernzerhof³⁸ was employed, together with the DFT-D2 method,⁴¹ to include long-range, two-body dispersion corrections (previous studies demonstrated the importance of such corrections).^{39,40} In the DFT-D2 scheme⁴¹ dispersion-corrections are described in terms of damped atom–atom $C_6^{AB} \cdot R_{AB}^{-6}$ terms, where R_{AB} is the distance between atoms A and B . A damping factor is engaged to avoid double counting and divergence at small R .⁴² The C_6^{AB} coefficients for describing dispersion between different atom types are defined in terms of the C_6^{AA} and C_6^{BB} coefficients by using the Lorentz–Bertholet combination rule.⁴³

The supercell for Na-MMT was developed starting from the structure of pyrophyllite,⁴⁴ which has no metal cation substitution and thus has neutral layers. A unit cell with [Al₄O₈(OH)₄(Si₈O₁₂)] composition was used for pyrophyllite. The lattice parameters of the unit cell are: $a = 5.16$, $b = 8.97$, and $c = 9.37$ Å, and $\alpha = 91.5$, $\beta = 100.5$, and $\gamma = 89.6$ °. To prepare the MMT structural model, a triclinic $2 \times 1 \times 1$ supercell with one isomorphous octahedral Al³⁺/Mg²⁺ substitution per unit cell was employed. This introduces one negative charge for each O₂₀(OH)₄ unit, which is compensated by Na⁺ ion in the interlayer space. This produces a supercell with the formula Na₂[MgAl₃O₈(OH)₄(Si₈O₁₂)₂]. Γ point sampling of the Brillouin zone is adequate because of the large size of the unit cell.

In the DFT/MD calculations the number of water molecules in the interlayer region was varied from two to eight in the presence of one carbon dioxide molecule. The system was first

equilibrated using the isobaric–isothermal ensemble (*NPT*) with $T = 348.15$ K and $P = 130$ bar, conditions close to those existing in subsurface geological reservoirs and cap rocks and also to those used in CO_2 intercalation experiments in clays carried out at National Energy Technology Laboratory (NETL).¹⁹ Starting from initial structures relaxed using MD simulations with force fields (see Section 2.2), an equilibration time of 15 ps was employed, followed by 20 ps production runs using the microcanonical ensemble. The velocity Verlet algorithm was then used to update positions every 0.5 fs. To reduce the energy drift to 1 K/ps, the energy convergence tolerance for the electronic self-consistency cycle at each Born–Oppenheimer step was set to 10^{-6} eV. The atomic velocities were collected every 2 fs for up to 20 ps from production runs and used to calculate the velocity autocorrelation functions (VACF),⁴³ which, in turn, were used to calculate the power spectra. The velocity autocorrelation function for CO_2 was computed using the standard definition:

$$C(t) = \frac{1}{3N} \sum_i^{3N} v_i(0) \cdot v_i(t) \quad (1)$$

where $v_i(t)$ is the velocity of the i th CO_2 atom at time t and N is the number of molecules in the simulation.

2.2. MD Simulations Using a Classical Force Field. The force field calculations were carried out using the GROMACS package.⁴⁵ For the clay system, the Clayff force field¹² which consists of nonbonded (electrostatic and van der Waals) terms parametrized for use with layered minerals was used. In Clayff the pairwise energy between atoms i and j separated by a distance r_{ij} is given by:

$$E_{ij} = \frac{q_i q_j e^2}{4\pi\epsilon_0 r_{ij}} + 4\epsilon_{ij} \left[\left(\frac{\sigma_{ij}}{r_{ij}} \right)^{12} - \left(\frac{\sigma_{ij}}{r_{ij}} \right)^6 \right] \quad (2)$$

where q_i is the charge on atom i , e is the elementary charge of an electron, ϵ_0 is the vacuum permittivity, and ϵ_{ij} and σ_{ij} are the Lennard-Jones energy and distance parameters, respectively. The flexible SPC²⁵ model was engaged for the water molecules placed in the interlayer space and for the layer hydroxyl groups. For CO_2 , a recently developed flexible potential including intramolecular bond stretch and angle bend was used.⁴⁶ The general expression for the total potential energy is:

$$E_{\text{Total}} = E_{\text{Coul}} + E_{\text{VDW}} + E_{\text{Stretch}} + E_{\text{Bend}} \quad (3)$$

where harmonic potentials are used for the bond stretch and angle bend terms:

$$E_{\text{Stretch}} = \frac{1}{2} k_s (r_{ij} - r_0)^2 \quad (4)$$

and

$$E_{\text{Bend}} = \frac{1}{2} k_b (\theta_{ijk} - \theta_0)^2 \quad (5)$$

The optimized force field parameters for CO_2 , presented in Table 1, were combined with those in Clayff¹² to model CO_2 intercalation into hydrated MMT. The Lorentz–Berthelot mixing rule⁴³ was used to obtain the Lennard-Jones parameters for interactions between unlike atoms. The simulations were performed under periodic boundary conditions, with the long-range electrostatics treated by the particle–particle–particle–mesh (PPPM) Ewald method.⁴³ The cutoff radii for the nonbonded van der Waals interactions and for the Ewald

Table 1. Force Field Parameters for CO_2

nonbonding		bonding	
q_C	+0.6512 e	k_{CO}	8443 kJ/mol \AA^2
q_O	−0.3256 e	r_{CO}	1.162 \AA
ϵ_C	0.2340 kJ/mol	k_{OCO}	451.9 kJ/mol rad^2
ϵ_O	0.6683 kJ/mol	θ_{OCO}	180.0°
σ_C	2.800 \AA		
σ_O	3.028 \AA		

summation of the electrostatics were chosen to be 12 \AA , with switching distances starting from 11 \AA . Due to the use of cut-offs for the LJ interactions, long-range dispersion corrections for energy and pressure were applied.⁴⁵ The leapfrog algorithm⁴⁷ was used to update positions every 1 fs.

The general chemical formula used for the sodium montmorillonite is $\text{Na}_x\text{Mg}_x\text{Al}_{2-x}\text{Si}_4\text{O}_{10}(\text{OH})_2 \cdot n\text{H}_2\text{O}$, where the layer charge resides on the octahedral sheet (tetrahedral substitutions such as Al^{3+} for Si^{4+} can also occur but are not considered here). For the molecular dynamics simulations with the Clayff force field,¹² the MMT structural model was created by replicating a pyrophyllite unit cell with an isomorphous octahedral $\text{Al}^{3+}/\text{Mg}^{2+}$ substitution to produce a triclinic $8 \times 4 \times 4$ supercell (64 times larger than the supercell used for the DFT-based MD simulations). The negative charge introduced by the substitution is compensated by 96 sodium ions residing in the interlayers. The stoichiometry is $\text{Na}_{0.75}\text{Mg}_{0.75}\text{Al}_{3.25}(\text{OH})_4(\text{Si}_4\text{O}_{10})_2$ with a layer charge of 0.75 per $\text{O}_{20}(\text{OH})_4$ layer unit. This results in 5120 atoms constituting the clay phase. The carbon dioxide content was varied from 0.5 to 4 molecules per unit cell and the water content was varied from one to nine molecules per unit cell. The water/ CO_2 composition in the interlayer region is designated as X - Y , where X and Y are, respectively, the numbers of water and CO_2 molecules per unit cell. Particular emphasis is placed on scenarios with three and five water molecules per unit cell. The former composition provides a partially saturated water monolayer (with $d \sim 11.4$ \AA), which is close to that of the samples used to study the impact of CO_2 exposure to Na-MMT in high-pressure experiments.^{5,6} The latter composition gives a d -spacing of 12.2 \AA which corresponds to a fully saturated monolayer (1W).⁴ In the 1W state MMT structure demonstrates a sharp decrease in ability to capture dry CO_2 as reported in high-pressure X-ray diffraction experiments.^{5,6} Relaxation of MMT with intercalated species was performed using the *NPT* ensemble at $T = 348.15$ K and $P = 130$ bar as well as at $T = 300$ K and $P = 1$ bar to study the dependence of the basal spacing on pressure. Equilibration runs of 1 ns were carried out followed by 20 ns production runs in the *NPT* ensemble, with *semi-isotropic* pressure coupling permitting the z -dimension to fluctuate independently from the x and y directions. Pressure was controlled by a Parrinello–Rahman barostat^{48,49} with a relaxation time of 4 ps, and temperature was controlled by a N ose–Hoover thermostat^{50,51} with a relaxation time of 2 ps. A time step of 1 fs was used in the simulations.

The radial distribution function (RDF) for species B around A is calculated as:

$$G_{A-B}(r) = \frac{1}{4\pi\rho_B r^2} \frac{dN_{A-B}}{dr} \quad (6)$$

where ρ_B is the number density of species B and dN_{A-B} is the average number of type B particles lying in the region r to $r + dr$

from a type A particle. N_{A-B} is the coordination number for B around A.

To calculate the diffusion coefficients of the interlayer species, the Einstein relation was employed using equilibrated atomic trajectories from the NVT ensemble simulations with 1 ps sampling to evaluate the mean square displacement of the molecules and ions:

$$D = \lim_{t \rightarrow \infty} \frac{1}{6N_m t} \sum_{j=1}^{N_m} [r_j(t) - r_j(0)]^2 \quad (7)$$

where N_m is a number of a selected species and $r_i(t)$ is the center-of-mass position of the i th species at time t . The averages were over 4 ns trajectories. The diffusion coefficients were derived from the linear slope of the mean square displacement as a function of the simulation time. Different restart points in the analysis were taken to monitor convergence.

2.3. Experimental Section. Diffuse Reflectance Infrared Fourier-Transform Spectroscopy (DRIFTS). The clay samples used in this work were powders of SWy-2 (natural Na-rich-MMT from Wyoming) and STx-1b (natural Ca-rich-MMT from Texas) acquired from the Source Clays Repository.^{10,11} An FT-IR spectrometer (Thermo Electron Corporation, Model Nicolet 8700) with a Smart Collector and dual environmental chamber was used to obtain diffuse reflectance infrared spectra. The spectra were collected in a nitrogen flow-through environment, after eight hours of exposure of the clay samples to 1500 psig (~ 10 MPa) pressure of carbon dioxide at 55 °C. In each measurement, 100 scans were completed with 4 cm^{-1} resolution. KBr diffuse reflectance spectra were used as a background reference. More details on the experimental setup and execution can be found elsewhere.¹⁹

3. RESULTS AND DISCUSSION

3.1. Force Field Results. Figure 1 shows a schematic representation of the montmorillonite TOT layers and interlayer species (H_2O , CO_2 , Na^+) considered in this study. Figure 2 reports the expansion of the d -spacing of Na-MMT upon intercalation of water computed using molecular

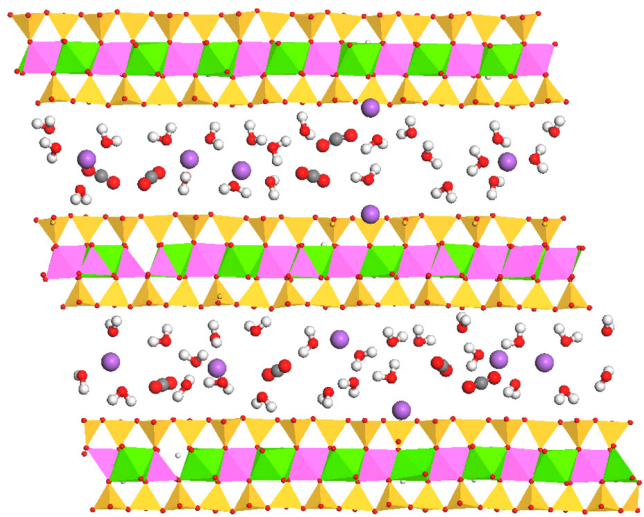


Figure 1. Schematic representation of the clay/water/ CO_2 system. Color designation: red balls – oxygens; purple – sodium ions; white – hydrogens; gray – carbon.

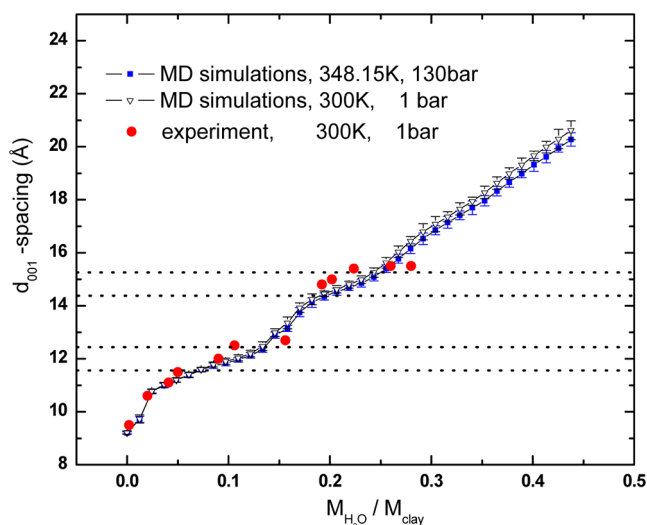


Figure 2. Swelling behavior of Na-montmorillonite clay upon hydration. Comparison of calculated and experimental results (red circles) from ref 4. Dotted lines indicate ranges of basal d -spacing corresponding to the 1W and 2W hydration states.

dynamics simulations with the Clayff force field.¹² Comparison with experimental data shows that the MD results closely reproduce the experimental trend in the d -spacing, displaying plateaus corresponding to formation of monolayer and bilayer water in the interlayer. It is important to note that it is a generally accepted paradigm among clay mineralogists that coexistence of different hydration states (0W, 1W, 2W) in a smectite sample is common even under controlled conditions.⁵² It is also generally accepted that fractional hydration states correspond to a sample with different integer hydration structures. For example, the diffuse character of the (00 l) reflections, at the transition between two discrete hydration states, and the asymmetric (001) peak profile provides evidence that the montmorillonite structure evolves gradually from one hydration state to the other through mixed-layer structures composed of discrete hydration states.^{53,54} Therefore, the experimental data outside of the ranges designated by the dotted lines in Figure 2 may have originated from a mixture of montmorillonite at different hydration states. In the simulations the structures corresponding to the intermediate d -spacing values were obtained from well-defined model systems with controlled amounts of water in the interlayer. Hydration levels intermediate between 0W and 1W and intermediate between 1W and 2W do provide equilibrated structures with parallel TOT clay layers as necessary to obtain a series of basal diffraction peaks. Thus our calculations suggest that smectite minerals could exist at fractional hydration states. However, it is possible that these are obscured in experimental diffraction studies by the mixed hydration states.

The spacing calculated for the P - T conditions employed in the NETL experiment ($T = 75$ °C and $P = 130$ bar)¹⁹ deviates only slightly from that calculated at $P = 1$ bar and lower temperature. Thus, the d -spacing is relatively insensitive to changes in pressure and temperature, with the degree of water content being the main factor controlling the extent of swelling. This is consistent with XRD-measurements of d -spacings showing that hydrate states are relatively stable with pressure.^{4,5,14}

DFT calculations have shown that a relative orientation of CO_2 in the interlamellar space of Na-MMT can be either

parallel to the clay surface (a global minimum) or nearly perpendicular.⁵⁵ The results of Gibbs ensemble Monte Carlo simulations using classical force fields revealed that dry CO₂ in Na-MMT is unstable except at large (>2W) *d*-spacing values.²⁷ In order to study CO₂ intercalation, force field MD simulations with the water content varied from one to nine water molecules per unit cell were performed. Figure 3 displays the calculated

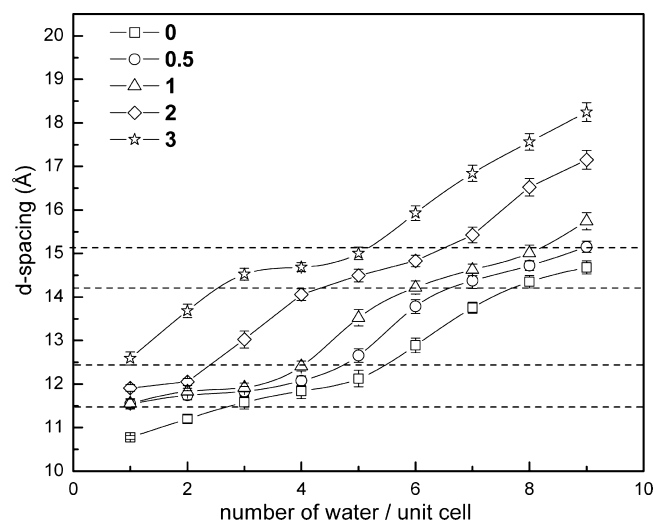


Figure 3. *d*-spacing as a function of number of water molecules at fixed numbers of CO₂ molecules per unit cell. Dashed lines indicate ranges of basal *d*-spacing corresponding to 1W and 2W hydration states.

interlayer distance as a function of the number of water molecules for selected numbers of intercalated carbon dioxide molecules per unit cell. The bottom curve, which reports the results in the absence of intercalated CO₂ molecules, serves as the reference. As seen in Figure 3, intercalation of CO₂ causes an expansion of the interlamellar spacing comparable to that caused by increasing hydration. Full monolayer coverage is achieved for five water molecules per unit cell, as well as for 4H₂O + 1CO₂, 2H₂O + 2CO₂, or 1H₂O + 3CO₂. In the latter two cases, the fact that $n\text{H}_2\text{O} + m\text{CO}_2 = 4$ rather than 5 reflects the larger size of the CO₂ molecule compared to H₂O. Similarly, full bilayer coverage can be achieved with compositions ranging from nine water molecules to three water molecules plus three CO₂ molecules. At a water content of six molecules per unit cell, the addition of a single CO₂ molecule per unit cell results in expansion of the *d*-spacing to a value close to that of the 2W state. However, the latter process appears to be thermodynamically unfavorable as intercalation of CO₂ was not observed in several *in situ* XRD studies^{5,6,14} on Na- and Ca-MMT with the initial *d*-spacing corresponding to the fully saturated 1W state (i.e., 5–6 H₂O molecules per unit cell). At *d*-spacing distances of ~14–15 Å (corresponding to the 2W state) a distinct plateau is observed for fixed CO₂ concentrations over a range of initial water content (Figure 3). For example, 8–0.5, 7–1, and 6–2 water–CO₂ compositions all have similar *d*-spacings. As a result, in the 2W hydration state CO₂ incorporation can displace water keeping the *d*-spacing nearly constant rather than further expanding the interlayer spacing.

To explore the distribution of the various species in the interlamellar space of the clay, density profiles were calculated for 3-Y and 5-Y compositions. Figures 4 and 5 display the resulting density profiles computed along the *z* axis

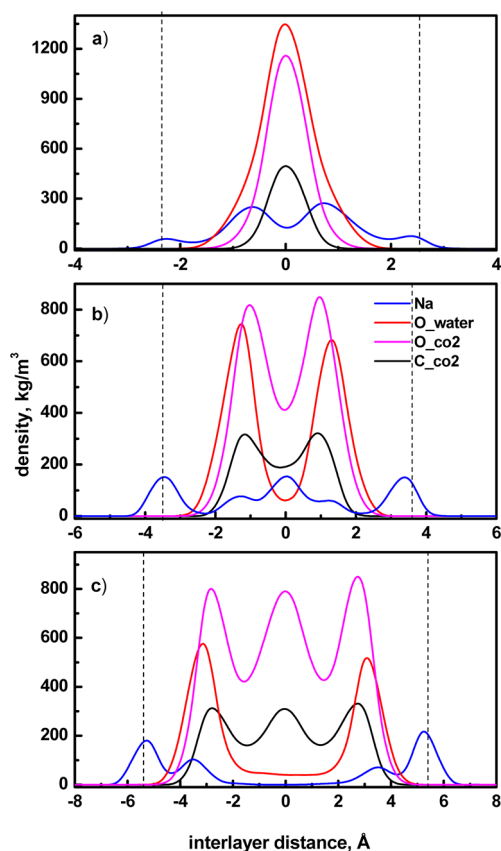


Figure 4. Density profiles along the interlayer distance perpendicular to the internal surfaces of Na-MMT showing distribution of the intercalated species for (a) 3–1, (b) 3–2, and (c) 3–4 compositions. Dashed lines designate the planes of basal oxygens.

(perpendicular to the clay surface) and averaged over the interlayer region of the simulation box. The amounts of CO₂ were chosen to induce *d*-spacing expansion toward the 1W, 2W, and 3W hydration states. The distributions confirm that H₂O and CO₂ molecules indeed form well-defined layered structures similar to pure 1W and 2W hydration states. Figure 4a reports the profiles for the 1W state, which, upon addition of one more CO₂ molecule per cell, starts to form the 2W state (Figure 4b). Figure 4b reports the profiles for a “nonsaturated” 2W system, while Figure 5b represents a fully saturated 2W. Figures 4c and 5c report the density profiles at the interlayer distances corresponding to the 3W hydration state. At those spacings (3W) the simulations show that the center layer is composed almost entirely of CO₂ molecules sandwiched between two layers of the CO₂/H₂O mixture.

The ability of water molecules to induce swelling in a stepwise fashion is related to the formation of an extended hydrogen bonding network and interaction of the water molecules with clay surface.⁴ The carbon dioxide can be expected to participate in interaction with water and clay surfaces. In this regard, it is instructive to consider the orientational behavior of CO₂ in the confining environment of MMT. This is accomplished by examining the distribution of angles between the CO₂ axial orientation and the axis perpendicular to the clay surfaces. Figure 6 reports this distribution computed using for each CO₂ molecule the C–O bond most nearly perpendicular to the surface at H₂O/CO₂ compositions corresponding to 1W, 2W, and 3W hydration states. At each state a normal distribution centered around 90°

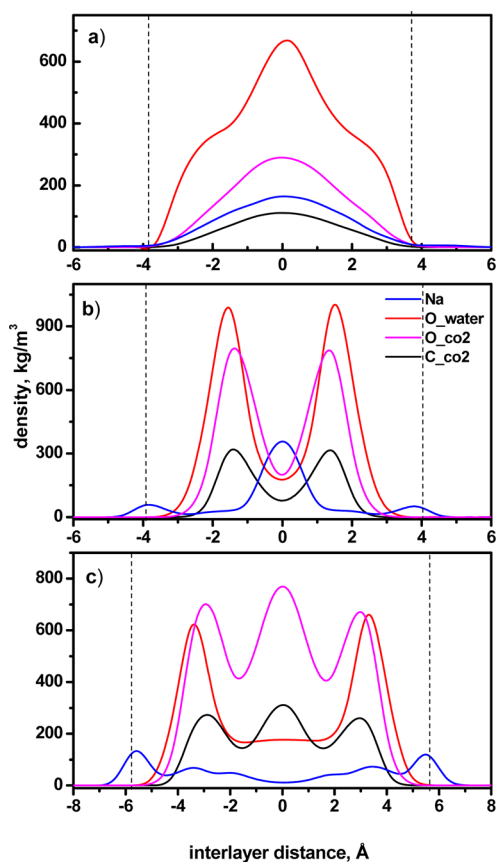


Figure 5. Density profiles along the interlayer distance perpendicular to the internal surfaces of Na-MMT showing distribution of the intercalated species for (a) 5–1, (b) 5–2, and (c) 5–4 compositions. Dashed lines designate the planes of basal oxygens.

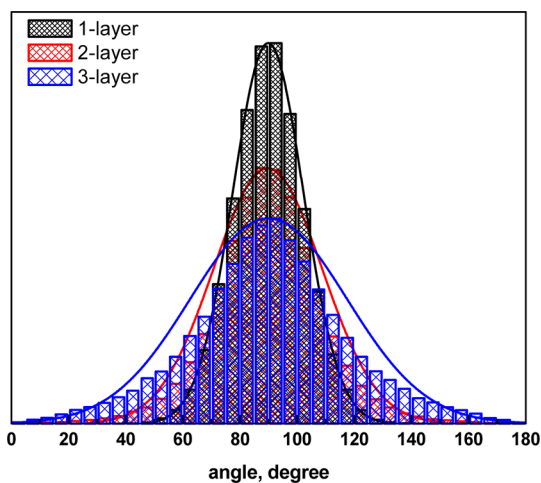


Figure 6. Histograms of angular distribution for CO₂ orientation relative to the axis perpendicular to clay surface. Data averaged over 30 CO₂ molecules for every composition during 4 ns.

is obtained, indicating that the carbon dioxide molecules are preferentially oriented parallel to the confining clay surfaces. With increasing number of water–CO₂ layers, the CO₂ molecules explore a wider range of angles consistent with greater rotational freedom in the interlayer. Inspection of the corresponding MD trajectories reveals that the CO₂ molecules display no specific coordination to the atoms comprising MMT. These data are consistent with experimental observations that

MMT has to be wetted in order to intercalate CO₂.^{5,6,14} Thus, the compositions providing the density profiles depicted in Figures 4c and 5c with a central CO₂ layer are likely to be unstable with respect to collapse to a more stable bilayer form (Figures 4b and 5b) by expelling CO₂ molecules or to expansion into the 3W hydration state by incorporating more water molecules.

As seen in Figures 4 and 5, pronounced changes occur in the density profiles of the Na⁺ ions with increasing CO₂ content. Specifically, the incorporation of CO₂ molecules into the interlayer region enhances the probability of finding Na⁺ ions near the surfaces, thus splitting the Na⁺ profiles into several peaks. The surface-bound sodium ions (inner-sphere adsorption) are coordinated above the centers of the hexagonal rings of silicon tetrahedra linked by shared basal oxygens. However, these ions retain strong interactions with nearby water molecules. In this regard, the amount of water should be an important factor determining the degree of ion adsorption. Indeed, comparison of Figures 4 and 5 shows that cation adsorption at the surface is less important in the systems having five water molecules per unit cell than in the systems with only three H₂O molecules per unit cell. To quantify the adsorption process the concentrations of the Na⁺ ions at the surfaces were calculated as a function of the carbon dioxide concentration. Figure 7 displays occupancy values of Na⁺ ions near the centers

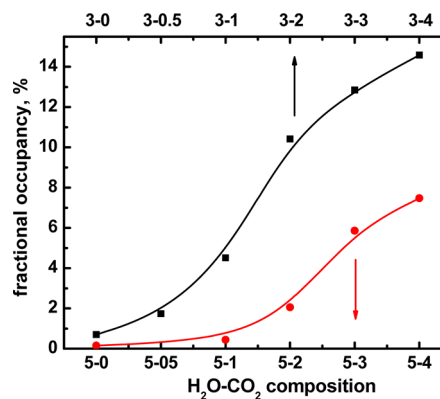


Figure 7. Fractional occupancy of the hexagonal sites on the internal clay surfaces by Na⁺ as a function of H₂O/CO₂ composition in the interlayer.

of the hexagonal rings as a percentage of a total number of the rings for the 3-Y and 5-Y compositions. To calculate these values the sodium atoms were counted as being adsorbed at the hexagonal rings when the ions had a residence time at the surface greater than 50% of the total simulation time. A Na⁺ ion was considered adsorbed at the surface if three and more distances between the sodium ion and basal oxygens become less than 2.9 Å. The adsorption of Na⁺ ions on the internal surfaces depends strongly on the water content, with the extent of surface adsorption being greater for the 3-Y than for 5-Y composition. The 3-Y and 5-Y composition plots are reminiscent of a typical adsorption isotherm showing increase of Na⁺ adsorbate concentration with increase of CO₂ content in the interlayer. The plot for the 5-Y composition reveals a more smooth behavior, with the preference for Na⁺ to stay solvated in the interlayer in the absence of CO₂ content. Increasing the carbon dioxide concentration promotes migration of the ions to the clay surfaces where they form inner-sphere surface complexes.⁵⁶ The adsorption of sodium ions at the clay

Table 2. Calculated Hydrogen Bond Lifetimes (τ , ps)^a

	composition (X-Y)*					
	3-0 (1L)	3-0.5 (1L)	3-1 (1L)	3-2 (2L)	3-3 (2L)	3-4 (3L)
$\tau_{\text{H}_2\text{O}-\text{H}_2\text{O}}$	7.36	9.31	15.28	12.21	6.28	5.92
$\tau_{\text{H}_2\text{O}-\text{CO}_2}$	-	6.48	8.65	2.77	2.64	1.71
$\tau_{\text{H}_2\text{O}-\text{clay}}$	20.25	12.98	13.54	6.25	4.21	3.69
	5-0 (1L)		5-1 (1L)	5-2 (2L)	5-3 (3L)	5-4 (3L)
$\tau_{\text{H}_2\text{O}-\text{H}_2\text{O}}$	11.76		9.97	5.88	8.36	5.24
$\tau_{\text{H}_2\text{O}-\text{CO}_2}$	-		2.4	0.68	1.84	0.31
$\tau_{\text{H}_2\text{O}-\text{clay}}$	5.15		7.22	2.17	4.57	1.43

^aThe number of layers is indicated in parentheses.

Table 3. Diffusion Coefficients ($\times 10^{-5}$ cm²/s) of Water, Carbon Dioxide Molecules, and Na⁺ Cations^a in the Interlayer Space of Na-montmorillonite

diffusion coef.	composition X-Y					
	3-0 (1L)	3-0.5 (1L)	3-1 (1L)	3-2 (2L)	3-3 (2L)	3-4 (3L)
$D^{\text{H}_2\text{O}}$	0.26 ± 0.02	0.26 ± 0.02	0.14 ± 0.02	0.24 ± 0.05	0.35 ± 0.03	0.68 ± 0.07
$D_{xy}^{\text{H}_2\text{O}}$	0.39 ± 0.03	0.39 ± 0.02	0.21 ± 0.02	0.36 ± 0.04	0.52 ± 0.07	1.01 ± 0.09
	0.28 ^b ; 1.0 ± 0.1 ^c		0.32(2) ^c			
	5-0 (1L)		5-1 (2L)	5-2 (2L)	5-3 (3L)	5-4 (3L)
$D^{\text{H}_2\text{O}}$	0.21 ± 0.02		0.47 ± 0.06	0.53 ± 0.02	0.52 ± 0.01	0.72 ± 0.06
$D_{xy}^{\text{H}_2\text{O}}$	0.30 ± 0.02		0.70 ± 0.08	0.80 ± 0.03	0.80 ± 0.06	1.08 ± 0.08
	0.28 ^b ; 1.0 ± 0.1 ^c					
	3-0 (1L)	3-0.5 (1L)	3-1 (1L)	3-2 (2L)	3-3 (2L)	3-4 (3L)
D^{CO_2}		0.16 ± 0.01	0.12 ± 0.01	0.92 ± 0.05	1.10 ± 0.07	2.23 ± 0.15
$D_{xy}^{\text{CO}_2}$		0.23 ± 0.01	0.18 ± 0.01	1.38 ± 0.08	1.65 ± 0.08	3.12 ± 0.17
			0.17(2) ^d			
	5-0 (1L)		5-1 (2L)	5-2 (2L)	5-3 (3L)	5-4 (3L)
D^{CO_2}			0.55 ± 0.05	0.77 ± 0.07	1.49 ± 0.25	2.82 ± 0.13
$D_{xy}^{\text{CO}_2}$			0.82 ± 0.05	1.15 ± 0.11	2.24 ± 0.34	4.23 ± 0.17
	3-0 (1L)	3-0.5 (1L)	3-1 (1L)	3-2 (2L)	3-3 (2L)	3-4 (3L)
D^{Na^+}	0.04 ± 0.01	0.08 ± 0.01	0.07 ± 0.01	0.05 ± 0.01	0.06 ± 0.01	0.10 ± 0.02
$D_{xy}^{\text{Na}^+}$	0.06 ± 0.02	0.12 ± 0.01	0.10 ± 0.02	0.08 ± 0.02	0.25 ± 0.17	0.48 ± 0.22
			0.13(2) ^d		0.08 ± 0.01	0.12 ± 0.03
					0.37 ± 0.26	0.58 ± 0.31
	5-0 (1L)		5-1 (2L)	5-2 (2L)	5-3 (3L)	5-4 (3L)
D^{Na^+}	0.12 ± 0.01		0.17 ± 0.04	0.21 ± 0.01	0.13 ± 0.03	0.10 ± 0.01
					0.21 ± 0.09	0.26 ± 0.14
$D_{xy}^{\text{Na}^+}$	0.17 ± 0.02		0.24 ± 0.04	0.31 ± 0.01	0.19 ± 0.04	0.14 ± 0.01
					0.32 ± 0.12	0.39 ± 0.11

^aItalic font is used to designate coefficients calculated for sodium cations solvated by water in the interlayer space. D_{xy} denotes lateral diffusion coefficients for motion parallel to clay surfaces. Number of layers is given after a composition notation in the parentheses. ^bRef 59. ^cRef 60. ^dRef 23.

surfaces increases the hydrophobicity of the surfaces since the ions effectively shield the basal oxygens from hydrogen bonding with water molecules. This process could also be responsible for observed dewetting and increased contact angles on mica and silica surfaces during scCO₂ invasion under high ionic strength of brine.⁵⁷

In order to characterize how the various interactions impact the hydrogen bonding, hydrogen-bond lifetimes were computed following the approach described in ref 58. Table 2 reports the calculated hydrogen-bond lifetimes for water–clay, water–water, and water–carbon dioxide pairs at different carbon dioxide concentrations and two levels of water content. In general, the longest lived hydrogen bonds are those between water molecules followed by water–clay and then water–CO₂. This is consistent with the results of our recent investigation of water loading on the pyrophyllite surface that displayed stronger water–water than water–surface interactions.⁴⁰

Increased intercalation of carbon dioxide is accompanied by decreased H-bond lifetimes for all three types of interactions. This indicates that as the interlayer space is expanded, the molecular coordination becomes less structured (Table 2, Figure 6). Thus, expansion of the confining space to accommodate more CO₂ molecules translates into a more orientationally disordered arrangement of the interlayer water and carbon dioxide molecules.

3.2. Diffusion of the Interlayer Species in Na-montmorillonite. Table 3 reports the diffusion coefficients for interlayer species computed in this work as well as those obtained from earlier simulations and experimental measurements in similar systems. The calculated values are reported for both diffusion in 3D space and for diffusion parallel to the clay surfaces. In the confining environment of nanochannels the lateral diffusion coefficients are more relevant. The data reported in Table 3 show that for both water and carbon

dioxide molecules the diffusivities for lateral motion are about 30% greater than those for three-dimension motion. Moreover, the diffusion coefficients of both CO₂ and H₂O increase with increasing concentration of CO₂ due to the associated expansion of the interlayer space. The diffusion coefficients of water computed for the systems without CO₂ (3–0 and 5–0) are in close agreement with the experimental values for interlayer water in MMT obtained using QENS spectroscopy⁵⁹ and neutron spin echo for synthetic Na-hectorite,⁶⁰ a trioctahedral smectite with isomorphous substitution in the octahedral sheet that displays the similar swelling properties as MMT and has comparable diffusion coefficients.⁶¹ The diffusion coefficients of H₂O and CO₂ in the interlayer of Na-MMT calculated for the 3–1 composition are in agreement with those computed by Botan et al.²³ for a similar composition. Formation of the second and third water/CO₂ layers induced by CO₂ intercalation leads to stepwise increases in diffusivity of carbon dioxide compared to the values obtained for the monolayer arrangement. The effect of clay swelling on the diffusion coefficients is more pronounced for CO₂ than for water. For example, for the 3-Y composition the change from mono- to the bilayer arrangement is accompanied by nearly an order of magnitude increase of the CO₂ diffusion coefficients, while the corresponding change for water is only about a factor of 2 (Table 3). The greater impact of the interlayer spacing on the CO₂ diffusivity can be understood in terms of the preferred parallel orientation of the CO₂ molecules relative to the clay surface.

At basal *d*-spacings corresponding to three layers (where the central layer comprised solely of CO₂ molecules is sandwiched between two CO₂/water layers), the lateral diffusion coefficient for CO₂ attains a value of $4.23 \pm 0.17 \times 10^{-5}$ cm²/s. This value comprises contributions from both the CO₂ in water layers and the central CO₂ layer and is comparable to that measured for diffusion of CO₂ in bulk water at $5.40 \pm 0.10 \times 10^{-5}$ cm²/s (*T* = 348.15 K).⁶³ Expansion of the interlayer space due to an increase of the carbon dioxide content and subsequent formation of multilayers formed by interlayer species leads to an increase in diffusion coefficients of water (Table 3). The calculated diffusion constants of H₂O in MMT are in good agreement with measured diffusion constants for water in clay interlayer spaces. The measured diffusion coefficient of water in the bulk at *T* = 343 K is 5.65×10^{-5} cm²/s⁶² which is more than an order of magnitude greater than that for water confined between clay layers.

In the case of Na⁺ ions, direct comparison of the computed and experimental values of the diffusion constants can be misleading since measured ionic mobilities in montmorillonite samples can have contributions from pores and external surfaces as well as from the interlayer spaces depending on experimental conditions and ionic strength.^{64,65} Kozaki et al.^{64,65} reported a diffusion constant of 1.8×10^{-6} cm²/s for interlayer sodium ions in the 2W hydration state of MMT at *T* = 323 K and 0.1–0.3 M concentrations. This value is close to the computed diffusion constants of sodium ions in the interlayer space (Table 3). The intercalation of CO₂ has only a moderate effect on the diffusion coefficient of the sodium ions. However, the computed diffusion constants include contributions from the surface-adsorbed ions that grow in importance as the CO₂ content increases (Figures 4 and 5). We have also carried out calculations where diffusion of the interior sodium ions was separated from contributions from surface-bound Na⁺ ions. Not surprisingly, the diffusion coefficients for nonsurface

bound Na⁺ ions are much larger than those computed for total Na⁺ ions for compositions with high CO₂ content (Table 3). Such behavior is attributed to increased adsorption of Na⁺ at the surface as CO₂ concentration increases (Figure 7).

3.3. Infrared Spectra of Carbon Dioxide Trapped in Hydrated Na-Montmorillonite. CO₂ trapped in MMT produces a distinctive infrared reflectance spectrum.^{16,17,19} Figure 8 compares the asymmetric stretching region of Fourier

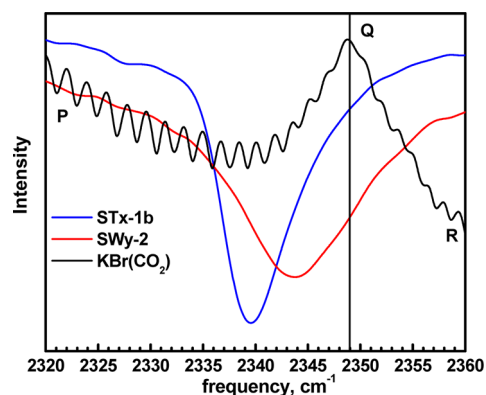


Figure 8. FT-IR diffuse-reflectance spectra of CO₂-treated smectite clay powders, Ca-MMT (STx-1b) and Na-MMT (SWy-2). KBr reflectance spectra were used for background subtraction. The vertical line marks the position of CO₂ asymmetric stretch fundamental (ν_3) for the gas phase; P, Q, and R branches represent the rovibrational coupling.

transform infrared spectra of gaseous CO₂ and of CO₂ trapped in Ca-MMT (STx-1b) and Na-MMT (SWy-2) clays. The gas-phase CO₂ molecule has rotational–vibrational sorption bands even though it has a zero permanent dipole. This is a consequence of the asymmetric (ν_3) stretch and bending modes inducing oscillating dipole moments. The selection rule for the band involving excitation of ν_3 is $\Delta J = \pm 1$ corresponding to P and R branches (where *J* is the rotational quantum number). The Q branch with $\Delta J = 0$ is forbidden and deduced to occur at ~ 2349 cm^{−1} (Figure 8, the vertical line). For CO₂ intercalated in a clay phase the selection rule that makes the Q-branch forbidden in the gas phase is lifted, and the spectra reveal a strong signal due to the CO₂ asymmetric stretch vibrational mode.⁶⁶ Rotational states of adsorbed molecules are frustrated by orientation-dependent perturbations within the surface potential wells^{67,68} and the rovibrational P, Q, and R branches collapse into a broad vibrational band, which is characteristic of physisorption.⁶⁹ The peak maximum is red-shifted by 5 cm^{−1} in Na-MMT and by 10 cm^{−1} in Ca-MMT relative to that of the fundamental of gaseous CO₂. These small frequency shifts indicate that carbon dioxide molecules are not engaged in strong interactions.

Classical molecular dynamics simulations were carried out with the Clayff force field¹² to compute the power spectra of CO₂ intercalated in Na-MMT with (H₂O)_{*n*}(CO₂)_{*m*} compositions of *n* = 1–9 and *m* = 1–4 per unit cell. These calculations provide a frequency of the CO₂ asymmetric stretch vibration essentially identical to that of the gas-phase molecule calculated using the same theoretical method. The failure of these simulations to predict a red shift of the CO₂ asymmetric stretch vibration is indicative of a deficiency in the force field. This led us to calculate also the power spectra using DFT-based MD simulations. Details of these calculations are given in Section

2.1 The supercell employed is comprised of two unit cells and contains one CO₂ molecule and two to eight water molecules in the interlayer region. The calculated power spectra are reported in Figure 9 from which it is seen that the calculated

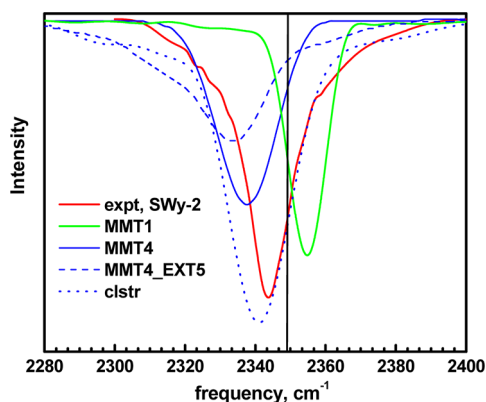


Figure 9. Comparison of the FT-IR asymmetric stretch mode for CO₂ intercalated into Na-MMT (expt, SWy-2) with the signal predicted using the power spectra for Na-MMT with 4 H₂O and 0.5 CO₂ molecules per unit cell (MMT4); with 1 H₂O and 0.5 CO₂ molecules per unit cell (MMT1); with 4 H₂O and 0.5 CO₂ molecules per unit cell with interlayer distance increased by 5 Å (MMT4_EXT5); and for a cluster of water and CO₂ molecules (clstr, see the text). The adjustment coefficient is 0.9941. The vertical line marks the CO₂ asymmetric stretch fundamental for the gas phase.

asymmetric stretch vibration of CO₂ is shifted 6 cm⁻¹ to the blue in MMT1 and 11 cm⁻¹ to the red in MMT4 compared to the corresponding gas-phase fundamental. For the systems incorporating intermediate numbers of water molecules the calculated value of the CO₂ asymmetric stretch frequency resides between these limits. This demonstrates that the hydration level strongly affects the direction and magnitude of the frequency shift. Inspection of the snapshots from the simulation trajectory of the MMT1 system reveals that the CO₂ molecule is primarily coordinated to a sodium cation due to insufficient number of water molecules to efficiently hydrate the cations. The blue shift calculated for CO₂ interacting with a sodium cation is consistent with the experimental results for CO₂-cation complexes.^{20–22} Increasing water content leads to formation of a hydration shell and release of CO₂ from coordination with the interlayer Na⁺ ions, which, in turn, leads to a red shift of the asymmetric stretch vibration.

To gain additional insight into the role of the CO₂-H₂O interactions, the O_w-C and H_w-O_{CO₂} radial distribution functions (RDFs) were calculated. Figure 10a,b reports the RDFs for O_w-C and H_w-O_{CO₂} pairs obtained from DFT-based and Clayff MD simulations at various H₂O/CO₂ compositions. The H_w-O_{CO₂} RDFs from the simulations using the force field display a shoulder near 2.3 Å, indicating formation of H-bonds between H₂O and CO₂. However, this shoulder recedes as the water content increases, and it is absent in the DFT-based MD simulations. Kumar et al.⁷⁰ using Car-Parrinello MD simulations obtained a similar H_w-O_{CO₂} RDF consistent with little H-bonding between water and CO₂ molecules. The O_w-C RDF from the force field simulations displays a weak shoulder near 3.1 Å, while that from DFT-based MD simulations has a pronounced peak around 2.9 Å which is close to the value reported for the global minimum of the CO₂-H₂O complex at

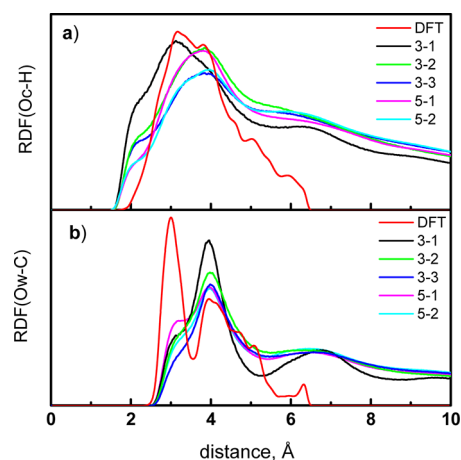


Figure 10. (a) Oxygen (CO₂)-hydrogen (H₂O), and (b) oxygen (H₂O)-carbon radial distribution functions for Na-MMT at various compositions of H₂O and CO₂. The RDFs designated as X-Y were obtained from classical MD simulations. The RDF marked as DFT was obtained from the DFT/MD simulations on the Na-MMT system with 4 H₂O and 0.5 CO₂ molecules per unit cell.

the CCSD(T) level of theory.^{71,72} These results indicate a possible shortcoming in the description of the CO₂-water interactions in the force field calculations. Recently, Vlcek et al.⁷³ reported “polarization-corrected” LJ parameters for the unlike pair interactions in water/carbon dioxide mixtures and used SPC/E and EPM2 force fields to simulate CO₂ in liquid water. The resulting RDFs closely resemble those obtained from our classical force field simulations of CO₂ in hydrated MMT. Thus, the deficiency in the force field appears not to be related to the use of combination rules in determining the van der Waals parameters for CO₂-water. It could reflect the inadequacy of a 3-point charge model for representing the electrostatic potential of CO₂.

In order to further explore the effect of the confining environment on the frequency of the CO₂ asymmetric stretch vibration, DFT-based MD simulations were also conducted on the MMT4 system with the basal distance extended by 5 Å. The extended interlayer space diminishes the effect of the basal oxygens and allows for a more flexible rearrangement of water molecules and interlayer ions during interaction with CO₂. For this system the asymmetric stretch vibration appears at 2334 cm⁻¹, red-shifted by 15 cm⁻¹ relative to the gas-phase value (Figure 9). This result provides further evidence of the pivotal role of the water molecules in the confining environment of clay in determining the frequency of the CO₂ asymmetric stretch fundamental. DFT-based MD simulations were also performed using a simulation box with a cluster of eight water molecules and one CO₂ molecule, and having dimensions corresponding to the interlayer space of the equilibrated MMT4 system. The frequency of the CO₂ asymmetric stretch is calculated to occur 8 cm⁻¹ to the red from the fundamental vibration of the gas-phase CO₂ molecule (Figure 9). This is consistent with the peak in the experimental band of the asymmetric stretch showing a red shift about 6 cm⁻¹ relative to the gas-phase molecule.^{74,75}

To explore the origin of the red shift in the asymmetric stretch vibration of CO₂ intercalated in Na-MMT, snapshots were extracted from a DFT-based MD trajectory. The sampled structures show that the CO₂ molecule is surrounded by water molecules, many of which have OH groups that point toward

the O atoms of the CO₂ molecule. In several of the snapshots, the C–O bonds in the carbon dioxide molecule are slightly elongated in comparison with those of the gas-phase molecule (1.167 Å). Selected CO₂ molecules were then extracted and their vibrational frequencies were calculated at the B3LYP/aug-cc-pVDZ level of theory. As expected, the asymmetric stretch vibration is red-shifted in the distorted molecules compared to the equivalent vibrational mode of the optimized gas phase CO₂ molecule computed at the same level of theory. The frequency shift correlates in a linear manner with the extent of the distortion as seen from Figure 11. The insert 1 in Figure 11

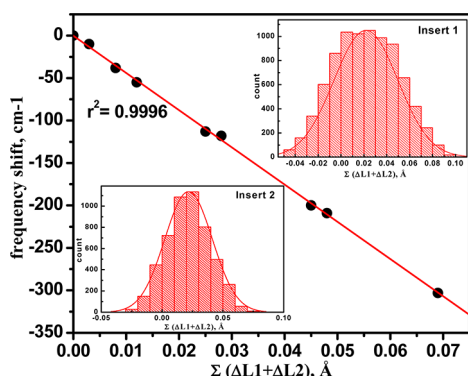


Figure 11. Correlation between a red shift of the asymmetric stretch vibration and a corresponding sum of incremental deviation of the bond lengths ($\Delta L1+\Delta L2$) for the CO₂ monomer relative to the gas-phase value. Insert 1 shows a histogram of geometry deviation values for CO₂ monomer in MMT4. The histogram data were obtained from a 15 ps DFT/MD trajectory. Insert 2 shows a histogram of geometry deviation values for CO₂ monomer in a cluster with eight water molecules in a simulation box (Figure 9 “clstr” and related text). The histogram data were obtained from a 10 ps DFT/MD trajectory.

reveals a histogram of the deviation of C–O bond lengths from the gas-phase value for MMT4 (Figure 9). The data shows that a normal distribution is centered around 0.02 Å indicating stretch of the bonds in the interlayer region of montmorillonite. A similar trend is found for the neutral cluster of water and a carbon dioxide molecule (Insert 2, Figure 11). These results provide strong evidence that the observed red shift is primarily due to geometry distortions of the CO₂ molecule induced by the water molecules. In several cases with large CO bond length increases and large red shifts of the asymmetric stretch vibration, all H–O(CO₂) distances are greater than 4 Å, strongly suggesting that it is electric field effects that are primarily responsible for the observed red shift. This also suggests that in the reported experiments^{15–17,19} hydration of CO₂ in the interlayer space is sufficient to form a solvation shell and preclude a direct interaction of CO₂ with sodium cations, which would act so as to cause a blue-shift.^{20–22} Remarkably, a similar red shift in the stretch fundamental was found by Rode et al.⁷⁵ in their mixed *ab initio*/force field MD simulations of carbon dioxide in water.

These results explain why the classical MD simulations did not predict a red shift for the intercalated carbon dioxide. Specifically, the force field employed uses a harmonic C–O stretch term, whereas it is necessary to include an anharmonic C–O stretch term to account for the frequency shift accompanying the stretch of the CO bonds upon hydration. This deficiency can be readily remedied, for example, by

adopting a Morse-type potential to describe the C–O stretch potential.

4. CONCLUSIONS

One option for CO₂ storage is to use subsurface geological brine aquifers bound by low-permeability sealing cap rocks. Cap rock is often enriched with expandable clay minerals, and understanding the interaction between clay minerals, brines, and injected CO₂ is crucial for predictions of the natural seal integrity and site selection for long-term CO₂ storage. The integrity of the cap rock is important because CO₂, being more buoyant than saline water and oil, will tend to migrate above these relatively immiscible fluids.

Experimental measurements show that trapping of carbon dioxide in Na- and Ca-montmorillonite leads to a red shift in the asymmetric stretch frequency of the CO₂ molecule. DFT-based MD simulations were carried out to explain the origin of this red shift. The simulations reproduce the experimentally observed red shift and identify electric-field-induced elongation of the CO bonds of CO₂ as being primarily responsible for the frequency shift.

Force field based molecular dynamics simulations were engaged to characterize the clay–water–CO₂ systems at pressure and temperature relevant to geological carbon sequestration. The simulations show that the degree of induced swelling caused by intercalation of CO₂ strongly depends on the initial water content in the interlayer space. Accumulation of CO₂ in the interlayer with humidity levels below those corresponding to the 1W hydration state first produces structures with basal *d*-spacings equivalent to 1W. Further carbon dioxide load promotes a stepwise expansion of the *d*-spacing to values equal to higher hydration states (2W and 3W). At water and CO₂ concentrations that give rise to mono- or bilayer arrangements in the interlayer region, the CO₂ molecules are preferentially oriented parallel to the clay surfaces. The hydrogen bond lifetimes are longest for H₂O–H₂O interactions followed by H₂O–O_{basal}, then by H₂O–CO₂. An important finding is that increasing the concentration of CO₂ promotes migration of the positively charged sodium ions to the clay basal surfaces. Sodium cations are found to absorb reversibly at the centers of hexagonal rings and to form surface complexes that contribute to charge screening of the electrical layer and acting so as to increase the hydrophobicity of the surface. This process could be related to the increase of contact angle and dewetting on mica and silica surfaces during CO₂ invasion reported in series of experiments under conditions of high ionic strength of electrolyte.⁵⁷ Thus, intercalation of CO₂ within smectite minerals in brine aquifers can cause significant changes in the clay phase *d*-spacing and modify wetting properties of the clay surfaces.

■ AUTHOR INFORMATION

Corresponding Author

*E-mail: Evgeniy.Myshakin@netl.doe.gov.

Notes

Disclaimer. This project was funded by the Department of Energy, National Energy Technology Laboratory, an agency of the United States Government, through a support contract with URS Energy & Construction, Inc. Neither the United States Government nor any agency thereof, nor any of their employees, nor URS Energy & Construction, Inc., nor any of their employees, makes any warranty, expressed or implied, or

assumes any legal liability or responsibility for the accuracy, completeness, or usefulness of any information, apparatus, product, or process disclosed, or represents that its use would not infringe privately owned rights. Reference herein to any specific commercial product, process, or service by trade name, trademark, manufacturer, or otherwise, does not necessarily constitute or imply its endorsement, recommendation, or favoring by the United States Government or any agency thereof. The views and opinions of authors expressed herein do not necessarily state or reflect those of the United States Government or any agency thereof.

The authors declare no competing financial interest.

ACKNOWLEDGMENTS

This technical effort was performed in support of the National Energy Technology Laboratory's ongoing research in Subtask 4000.4.641.061.001.255 under the RES contract DE-FE0004000. Additional funding was provided by the Center for Frontiers of Subsurface Energy Security, an Energy Frontier Research Center funded by the U.S. Department of Energy, Office of Science, Office of Basic Energy Sciences under Award Number DE-SC-0001114. Sandia National Laboratories is a multiprogram laboratory managed and operated by Sandia Corporation, a wholly owned subsidiary of Lockheed Martin Corporation, for the U.S. Department of Energy's National Nuclear Security Administration under Contract DE-AC04-94AL85000.

REFERENCES

- (1) Carbon Storage. www.netl.doe.gov/technologies/carbon_seq/coreord/storage.html (accessed February 15, 2013).
- (2) Allen, P. A.; Allen, J. R. *Basin Analysis: Principles and Applications*, 2nd ed.; Blackwell Pub.: Malden, MA, 2005.
- (3) Abdou, M. I.; Ahmaed, H. E. Evaluation of Low-Solids Mud Rheological Behavior during Drilling Shale Formation and Their Effect on the Pay Zone Productivity. *Pet. Sci. Technol.* **2010**, *28*, 934–945.
- (4) Fu, M. H.; Zhang, Z. Z.; Low, P. F. Changes in the Properties of a Montmorillonite-Water System during the Adsorption and Desorption of Water: Hysteresis. *Clays Clay Miner.* **1990**, *38*, 485–492.
- (5) Giesting, P.; Guggenheim, S.; Koster van Groos, A. F.; Busch, A. Interaction of Carbon Dioxide with Na-exchanged Montmorillonite at Pressures to 640 bar: Implications for CO₂ Sequestration. *Int. J. Greenhouse Gas Control* **2012**, *8*, 73–81.
- (6) Schaefer, H. T.; Ilton, E. S.; Qafoku, O.; Martin, P. F.; Felmy, A. R.; Rosso, K. M. *In situ* XRD Study of Ca²⁺ Saturated Montmorillonite (STX-1) Exposed to Anhydrous and Wet Supercritical Carbon Dioxide. *Int. J. Greenhouse Gas Control* **2012**, *6*, 220–229.
- (7) Kwak, J. H.; Hu, J. Z.; Turcu, R. V. F.; Rosso, K. M.; Ilton, E. S.; Wang, C. M.; Sears, J. A.; Engelhard, M. H.; Felmy, A. R.; Hoyt, D. W. The Role of H₂O in the Carbonation of Forsterite in Supercritical CO₂. *Int. J. Greenhouse Gas Control* **2011**, *5*, 1081–1092.
- (8) Spycher, N.; Pruess, K.; Ennis-King, J. CO₂-H₂O Mixtures in the Geological Sequestration of CO₂. I. Assessment and Calculation of Mutual Solubilities from 12 to 100°C and up to 600 bar. *Geochim. Cosmochim. Acta* **2003**, *67*, 3015–3031.
- (9) Gaus, I. Role and Impact of CO₂-Rock Interactions during CO₂ Storage in Sedimentary Rocks. *Int. J. Greenhouse Gas Control* **2010**, *4*, 73–89.
- (10) Costanzo, P. M. Baseline Studies of the Clay Minerals Society Source Clays: Introduction. *Clays Clay Miner.* **2001**, *49*, 372–373.
- (11) Martin, R. T. *Data Handbook for Clay Materials and Other Non-Metallic Minerals*; van Olphen, H., Fripiat, J. J., Eds.; Pergamon Press: New York, 1979.
- (12) Cygan, R. T.; Liang, J.-J.; Kalinichev, A. G. Molecular Models of Hydroxide, Oxyhydroxide, and Clay Phases and the Development of a General Force Field. *J. Phys. Chem. B* **2004**, *108*, 1255–1266.
- (13) Marry, V.; Turq, P.; Cartailleur, T.; Levesque, D. Microscopic Simulation of Structure and Dynamics of Water and Counterions in a Monohydrated Montmorillonite. *J. Chem. Phys.* **2002**, *117*, 3454–3463.
- (14) Ilton, E. S.; Schaefer, H. T.; Qafoku, O.; Rosso, K. M.; Felmy, A. R. *In Situ* X-ray Diffraction Study of Na⁺ Saturated Montmorillonite Exposed to Variably Wet Super Critical CO₂. *Environ. Sci. Technol.* **2012**, *46*, 4241–4248.
- (15) Loring, J. S.; Schaefer, H. T.; Turcu, R. V. F.; Thompson, C. J.; Miller, Q. R. S.; Martin, P. F.; Hu, J.; Hoyt, D. W.; Qafoku, O.; Ilton, E. S.; Felmy, A. R.; Rosso, K. M. *In Situ* Molecular Spectroscopic Evidence for CO₂ Intercalation into Montmorillonite in Supercritical Carbon Dioxide. *Langmuir* **2012**, *28*, 7125–7128.
- (16) Romanov, V. N.; Cygan, R. T.; Howard, B. H.; Myshakin, E. M.; Guthrie, G. D. Mechanisms of CO₂ Interaction with Expansive Clay. In *Proceedings of the 2010 SEA-CSSJ-CMS Trilateral Meeting on Clays*, Seville, Spain, 8–10 June, 2010.
- (17) Romanov, V. N.; Howard, B. H.; Lynn, R. J.; Warzinski, R. P.; Hur, T. B.; Myshakin, E. M.; Lopano, C. L.; Voora, V. K.; Al-Saidi, W. A.; Jordan, K. D.; Cygan, R. T.; Guthrie, G. D. CO₂ Interaction with Geomaterials. In *American Geophysical Union Fall Meeting*; San Francisco, 13–17 December, 2010, H11J01.
- (18) Hur, T.-B.; Baltrus, J. P.; Howard, B. H.; Harbert, W. P.; Romanov, V. N. Carbonate Formation in Wyoming Montmorillonite under High Pressure Carbon Dioxide. *Int. J. Greenhouse Gas Control* **2013**, *13*, 149–155.
- (19) Romanov, V. N. Evidence of Irreversible CO₂ Intercalation in Montmorillonite. *Int. J. Greenhouse Gas Control* **2013**, *14*, 220–226.
- (20) Gregoire, G.; Duncan, M. A. Infrared Spectroscopy to Probe Structure and Growth Dynamics in Fe⁺-(CO₂)_n Clusters. *J. Chem. Phys.* **2002**, *117*, 2120–2130.
- (21) Walker, N. R.; Grieves, G. A.; Walters, R. S.; Duncan, M. A. The Metal Coordination in Ni⁺(CO₂)_n and NiO₂⁺(CO₂)_m Complexes. *Chem. Phys. Lett.* **2003**, *380*, 230–236.
- (22) Jaeger, J. B.; Jaeger, T. D.; Brinkmann, N. R.; Schaefer, H. F.; Duncan, M. A. Infrared Photodissociation Spectroscopy of Si⁺(CO₂)_n and Si⁺(CO₂)_nAr Complexes: Evidence for Unanticipated Intracuster Reactions. *Can. J. Chem.* **2004**, *82*, 934–946.
- (23) Botan, A.; Rotenberg, B.; Marry, V.; Turq, P.; Noetinger, B. Carbon Dioxide in Montmorillonite Clay Hydrates: Thermodynamics, Structure, and Transport from Molecular Simulation. *J. Phys. Chem. C* **2010**, *114*, 14962–14969.
- (24) Smith, D. Molecular Computer Simulations of the Swelling Properties and Interlayer Structure of Cesium Montmorillonite. *Langmuir* **1998**, *14*, 5959–5967.
- (25) Berendsen, H. J. C.; Postma, J. P. M.; van Gunsteren, W. F.; Hermans, J. *Intermolecular Forces*; Pullmann, B., Ed.; Reidel: Dordrecht, The Netherlands, 1981.
- (26) Harris, J. G.; Yung, K. H. Carbon Dioxide's Liquid-Vapor Coexistence Curve And Critical Properties as Predicted by a Simple Molecular Model. *J. Phys. Chem.* **1995**, *99*, 12021–12024.
- (27) Yu, Y.; Yang, X. Molecular Simulation of Swelling and Interlayer Structure for Organoclay in Supercritical CO₂. *Phys. Chem. Chem. Phys.* **2011**, *13*, 282–290.
- (28) Yang, X.; Zhang, C. Structure and Diffusion Behavior of Dense Carbon Dioxide Fluid in Clay-like Slit Pores by Molecular Dynamics Simulation. *Chem. Phys. Lett.* **2005**, *407*, 427–432.
- (29) Peng, X.; Zhao, J.; Cao, D. J. Adsorption of Carbon Dioxide of 1-Site and 3-Site Models in Pillared Clays: A Gibbs Ensemble Monte Carlo Simulation. *Colloid Interface Sci.* **2007**, *310*, 391–401.
- (30) Cole, D. R.; Chialvo, A. A.; Rother, G.; Vlcek, L.; Cummings, P. T. Supercritical Fluid Behavior at Nanoscale Interfaces: Implications for CO₂ Sequestration in Geologic Formations. *Phil. Magazine* **2010**, *90*, 2339–2363.
- (31) Cygan, R. T.; Greathouse, J. A.; Heinz, H.; Kalinichev, A. G. Molecular Models and Simulations of Layered Materials. *J. Mater. Chem.* **2009**, *19*, 2470–2481.
- (32) Sholl, D.; Steckel, J. A. *Density Functional Theory: A Practical Introduction*; John Wiley & Sons, Inc.: Hoboken, NJ, 2009.

- (33) CP2K program suite. www.cp2k.org (accessed February 15, 2013).
- (34) Marx, D., Hutter, J. *Ab Initio Molecular Dynamics: Basic Theory and Advanced Methods*; Cambridge University Press: Cambridge, U.K., 2009.
- (35) Goedecker, S.; Teter, M.; Hutter, J. Separable Dual-Space Gaussian Pseudopotentials. *Phys. Rev. B* **1996**, *54*, 1703–1710.
- (36) Krack, M. Pseudopotentials for H to Kr Optimized for Gradient-Corrected Exchange-Correlation Functionals. *Theor. Chem. Acc.* **2005**, *114*, 145–152.
- (37) VandeVondele, J.; Hutter, J. Gaussian Basis Sets for Accurate Calculations on Molecular Systems in Gas and Condensed Phases. *J. Chem. Phys.* **2007**, *127*, 114105–114109.
- (38) Perdew, J. P.; Burke, K.; Ernzerhof, M. Generalized Gradient Approximation Made Simple. *Phys. Rev. Lett.* **1996**, *77*, 3865–3868.
- (39) Voora, V. K.; Al-Saidi, Jordan, K. D. Density Functional Theory Study of Pyrophyllite and M-Montmorillonites (M = Li, Na, K, Mg, and Ca): Role of Dispersion Interactions. *J. Phys. Chem. A* **2011**, *115*, 9695–9703.
- (40) Zhang, G.; Al-Saidi, W. A.; Myshakin, E. M.; Jordan, K. D. Dispersion-Corrected Density Functional Theory and Classical Force Field Calculations of Water Loading on a Pyrophyllite(001) Surface. *J. Phys. Chem. C* **2012**, *116*, 17134–17141.
- (41) Grimme, S. Semiempirical GGA-type Density Functional Constructed with a Long-range Dispersion Correction. *J. Comput. Chem.* **2006**, *27*, 1787–1799.
- (42) Tkatchenko, A.; Scheffler, M. Accurate Molecular Van Der Waals Interactions from Ground-State Electron Density and Free-Atom Reference Data. *Phys. Rev. Lett.* **2009**, *102*, 073005-1–073005-4.
- (43) Allen, M. P.; Tildesley, D. J. *Computer Simulation of Liquids*; Clarendon Press: Oxford, U.K., 1987.
- (44) Lee, J. H.; Guggenheim, S. Single Crystal X-ray Refinement of Pyrophyllite-1Tc. *Am. Mineral.* **1981**, *66*, 350–357.
- (45) van der Spoel, D.; Lindahl, E.; Hess, B.; van Buuren, A. R.; Apol, E.; Meulenhoff, P. J.; Tieleman, D. P.; Sijbers, A. L. T. M.; Feenstra, K. A.; van Drunen, R.; Berendsen, H. J. C. Gromacs User Manual, version 4.5.4. www.gromacs.org (accessed February 15, 2013).
- (46) Cygan, R. T.; Romanov, V. N.; Myshakin, E. M. Molecular Simulation of Carbon Dioxide Capture by Montmorillonite Using an Accurate and Flexible Force Field. *J. Phys. Chem. C* **2012**, *116*, 13079–13091.
- (47) van Gunsteren, W. F.; Berendsen, H. J. C. A Leap-frog Algorithm for Stochastic Dynamics. *Mol. Simul.* **1988**, *1*, 173–185.
- (48) Parrinello, M.; Rahman, A. Polymorphic Transitions in Single Crystals: A New Molecular Dynamics Method. *J. Appl. Phys.* **1981**, *52*, 7182–7190.
- (49) Nóse, S.; Klein, M. L. Constant Pressure Molecular Dynamics for Molecular Systems. *Mol. Phys.* **1983**, *50*, 1055–1076.
- (50) Nóse, S. A Molecular Dynamics Method for Simulations in the Canonical Ensemble. *Mol. Phys.* **1984**, *52*, 255–268.
- (51) Hoover, W. G. Canonical Dynamics: Equilibrium Phase-Space Distributions. *Phys. Rev. A* **1985**, *31*, 1695–1697.
- (52) Ferrage, E.; Lanson, B.; Sakharov, B. A.; Drits, V. A. Investigation of Smectite Hydration Properties by Modeling of X-ray Diffraction Profiles. Part I. Montmorillonite Hydration Properties. *Am. Mineral.* **2005**, *90*, 1358–1374.
- (53) Sato, T.; Watanabe, T.; Otsuka, R. Effects of Layer Charge, Charge Location, and Energy Change on Expansion Properties of Dioctahedral Smectites. *Clays Clay Miner.* **1992**, *40*, 103–113.
- (54) Ferrage, E.; Kirk, C. A.; Cressey, G.; Cuadros, J. Dehydration of Ca-montmorillonite at the Crystal Scale. Part I: Structure Evolution. *Am. Mineral.* **2007**, *92*, 994–1000.
- (55) Myshakin, E. M.; Voora, V. K.; Saidi, W. A.; Jordan, K. D., unpublished results.
- (56) Bourg, I.; Sposito, G. Molecular Dynamics Simulations of the Electrical Double Layer on Smectite Surfaces Contacting Concentrated Mixed Electrolyte (NaCl–CaCl₂) Solutions. *J. Colloid Interface Sci.* **2011**, *360*, 701–715.
- (57) Wan, J.; Jung, J.; Kim, Y. Wettability Alternation upon Reaction with CO₂; Silica, Mica, and Calcite. In *Nanoscale Control of Geologic CO₂ Fall Symposium*, Lawrence Berkeley National Laboratory, Berkeley, CA, October 3–4, 2011.
- (58) van der Spoel, D.; van Maaren, P. J.; Larsson, P.; Timneanu, N. Thermodynamics of Hydrogen Bonding in Hydrophilic and Hydrophobic Media. *J. Phys. Chem. B* **2006**, *110*, 4393–4398.
- (59) Marry, V.; Malikova, N.; Cadene, A.; Dubois, E.; Durand-Vidal, S.; Turq, P.; Breu, J.; Longeville, S.; Zanotti, J.-M. Water Diffusion in a Synthetic Hectorite by Neutron Scattering—beyond the Isotropic Translational Model. *J. Phys.: Condens. Matter* **2008**, *10*, 104205.
- (60) Marry, V.; Dubois, E.; Malikova, N.; Durand-Vidal, S.; Longeville, S.; Breu, J. Water Dynamics in Hectorite Clays: Influence of Temperature Studied by Coupling Neutron Spin Echo and Molecular Dynamics. *Environ. Sci. Technol.* **2011**, *45*, 2850–2855.
- (61) Malikova, N.; Cadene, A.; Dubois, E.; Marry, V.; Durand-Vidal, S.; Turq, P.; Breu, J.; Zanotti, J.-M.; Longeville, S. Water Diffusion in a Synthetic Hectorite Clay Studied by Quasi-elastic Neutron Scattering. *J. Phys. Chem. C* **2007**, *111*, 17603–17611.
- (62) Thomas, W.; Adams, M. Measurement of the Diffusion Coefficients of Carbon Dioxide and Nitrous Oxide in Water and Aqueous Solutions of Glycerol. *Trans. Faraday Soc.* **1965**, *61*, 668–673.
- (63) Lindeberg, E. G. B.; Wessel-Berg, D. Vertical Convection in an Aquifer Column under a Gas Cap of CO₂. *Energy Convers. Manage.* **1997**, *38*, S229–S234.
- (64) Kozaki, T.; Fujishima, A.; Sato, S.; Ohashi, H. Self-Diffusion of Sodium Ions in Compacted Sodium Montmorillonite. *Nucl. Technol.* **1998**, *121*, 63–69.
- (65) Kozaki, T.; Liu, J.; Sato, S. Diffusion Mechanism of Sodium Ions in Compacted Montmorillonite under Different NaCl Concentration. *Phys. Chem. Earth* **2008**, *33*, 957–961.
- (66) Papousek, D.; Aliev, M. R. *Molecular Vibrational-Rotational Spectra: Theory and Applications of High Resolution Infrared, Microwave and Raman Spectroscopy of Polyatomic Molecules*; Elsevier Science, Ltd.: New York, 1982.
- (67) Brown, D. W.; Sokol, P. E.; Fitzgerald, S. A. Rotational Dynamics of n-H₂ in Porous Vycor Glass. *Phys. Rev. B* **1999**, *59*, 13258–13266.
- (68) Schaffert, J.; Cottin, M. C.; Sonntag, A.; Karacuban, H.; Bobisch, C. A.; Lorente, N.; Gauyac, J.-P.; Möller, R. Imaging the Dynamics of Individually Adsorbed Molecules. *Nat. Mater. Lett.* **2013**, *12*, 223–227.
- (69) Kono, H.; Ziv, A. R.; Lin, S. H. Theoretical Studies of Molecules Adsorbed on Solid Surfaces: I. Electronic Spectra. *Surf. Sci.* **1983**, *134*, 614–638.
- (70) Kumar, P. P.; Kalinichev, A. G.; Kirkpatrick, R. G. Hydrogen-Bonding Structure and Dynamics of Aqueous Carbonate Species from Car-Parrinello Molecular Dynamics Simulations. *J. Phys. Chem. B* **2009**, *113*, 794–802.
- (71) Garden, A. L.; Lane, J. R.; Kjaergaard, H. G. Counterpoise Corrected Geometries of Hydrated Complexes. *J. Chem. Phys.* **2006**, *125*, 144317/1–144317/6.
- (72) de Lange, K. M.; Joseph, R.; Lane, J. R. Explicit Correlation and Intermolecular Interactions: Investigating Carbon Dioxide Complexes with the CCSD(T)-F12 Method. *J. Chem. Phys.* **2011**, *134*, 034301/1–034301/9.
- (73) Vlcek, L.; Chialvo, A. A.; Cole, D. R. Optimized Unlike-Pair Interactions for Water–Carbon Dioxide Mixtures Described by the SPC/E and EPM2 Models. *J. Phys. Chem. B* **2011**, *115*, 8775–8784.
- (74) Garrett-Roe, S.; Hamm, P. Purely Absorptive Three-Dimensional Infrared Spectroscopy. *J. Chem. Phys.* **2009**, *130*, 164510–164519.
- (75) Moin, S. T.; Pribil, A. B.; Lim, L. H. V.; Hofer, T. S.; Randolf, B. R.; Rode, B. M. Carbon Dioxide in Aqueous Environment—A Quantum Mechanical Charge Field Molecular Dynamics Study. *Int. J. Quantum Chem.* **2011**, *111*, 1370–1378.